applied optics

# Investigation of a field-widened Mach–Zehnder receiver to extend Fe Doppler lidar wind measurements from the thermosphere to the ground

John A. Smith[1,2] and Xinzhao Chu[1,*]

[1]Cooperative Institute for Research in Environmental Sciences & Department of Aerospace Engineering Sciences, University of Colorado Boulder, 216 UCB, Boulder, Colorado 80309, USA
[2]e-mail: John.A.Smith@colorado.edu
*Corresponding author: Xinzhao. Chu@colorado.edu

Received 21 September 2015; revised 7 January 2016; accepted 8 January 2016; posted 8 January 2016 (Doc. ID 250458); published 19 February 2016

**A receiver employing a field-widened Mach–Zehnder interferometer (MZI) is investigated for extending the wind measurement range of a narrow-band Fe Doppler lidar operating at 372 nm from its existing measurement range in the mesosphere and lower thermosphere (MLT) down to near the ground. This design uses the multiple transmitted frequencies available from the base Fe Doppler lidar in combination with a novel MZI receiver to make a measurement of the Doppler shift that rejects the influence of atmospheric parameters such as the aerosol backscatter ratio, temperature, and pressure of the lidar volume and receiver parameters such as the geometric overlap, the chopper function, and any other factor affecting the proportion of the signal in both channels of the MZI equally. A ratio is constructed from the three frequencies and two channels of the interferometer that exhibits a measurement performance of 1.75 times the Cramer–Rao lower bound, which is comparable to the dual MZI (DMZ) while preserving the insensitivity to backscatter spectrum of the quad MZI (QMZ). In addition, we show how the use of multiple transmitted frequencies can yield a wind measurement wherein the accuracy is insensitive to the optical imperfection and misalignment of the MZI or any other factor that affects the contrast, though the precision is still impacted by the fringe contrast. Simply adding a second surface mirror of a particular thickness to the basic tilted MZI can allow the field of the MZI to be widened sufficiently for most resonance Doppler lidar receivers in operation today. Provided that the detection sensitivity in each channel is known, the original resonance fluorescence and Rayleigh scattering signals can be recovered by simply scaling and adding the contributions from both channels. Consequently, the wind and temperature from the MLT region and the temperature from the Rayleigh region can be derived alongside the Rayleigh Doppler wind measurement without compromising the measurement precision. Using actual data obtained recently from a Major Research Instrumentation Fe Doppler lidar, we show the expected measurement performance and some potential scientific avenues for this embodiment of a "whole-atmosphere" lidar system.** 

***OCIS codes:*** (280.3640) Lidar; (010.3640) Lidar; (120.3180) Interferometry; (010.1080) Active or adaptive optics.

http://dx.doi.org/10.1364/AO.55.001366

## 1. INTRODUCTION

The concept of a "whole atmosphere lidar" was first proposed in 2008 at the 24th International Laser Radar Conference [1], and then evolved into the "Whole Atmosphere Lidar Observatory" advocated in the National Research Council 2013–2022 Decadal Strategy for Solar and Space Physics [2]. A whole atmosphere lidar would be used to profile key parameters (e.g., winds and temperatures) through the complete atmosphere column to help address the whole atmosphere sciences that are being promoted by the development of the whole atmosphere community climate model [3], the whole atmosphere model [4], and many other general circulation and chemical climate models [5]. The originally proposed lidar would profile both the wind and temperature from the ground to 120 km [1] with temporal and spatial resolutions sufficient to make useful characterizations of Earth's neutral atmosphere in an extended portion. Recently, layers of neutral metals (Fe, Na, and K) have been observed up to nearly 200 km [6–11], opening up the possibility of extending

lidar measurements of wind and temperature deeper into the thermosphere. Encouraged by these findings, the Observatory for Atmosphere-Space Interaction Studies (OASIS) initiative was formed by the Coupling, Energetics and Dynamics of Atmosphere Regions (CEDAR) community with the goal of extending these measurements up to ∼1000 km using a suite of lidars sharing an 11 m class telescope [12]. Such whole atmosphere lidar measurements would greatly advance our understanding of the complex, coupled mechanisms and feedback processes that govern our planetary atmosphere and are essential to sustaining life.

Resonance-fluorescence lidars, by exploiting the metal layers or other atomic/molecular species as tracers while acting as a Rayleigh lidar below the metal layers, provide the largest altitude coverage among lidars to date. This capability has most recently been demonstrated by an Fe Boltzmann lidar at McMurdo Station, Antarctica, where temperature measurements were made from 30 to nearly 170 km [6,7]. Consequently, resonance-fluorescence lidar is one of the best choices for a whole atmosphere lidar. In particular, modern resonance-fluorescence Doppler lidars can directly measure neutral winds and temperatures well into the thermosphere via probing the Doppler frequency shift and broadening the absorption lines of the neutral, unbound metal atoms such as Fe, Na, and K. Due to their high column abundance in the mesosphere and lower thermosphere (MLT), Fe and Na Doppler lidars are more attractive than other metal Doppler lidars. The UV wavelength and typically high pulse energy of Fe resonance transmitters make the Fe Doppler lidars more capable as Rayleigh lidars [13], so temperatures below the metal layers can be inferred with the Rayleigh integration technique [14].

To address wind measurements below the metal layers, in this study, we propose the addition of a frequency discriminator, comprised of a field-widened Mach–Zehnder interferometer (MZI), to the receiver system of an Fe Doppler lidar operating at multiple frequencies to discern the Doppler shift from Rayleigh scattering. An Fe Doppler lidar equipped with such an instrument would be especially well suited to fulfilling the above-mentioned needs and addressing the so-called "radar gap" in the statically stable region from 30–60 km. Despite the potential scientific benefits and the utility to current and future whole atmosphere models [3–5], routine wind profiling through the complete atmospheric column remains elusive for a single instrument and usually requires campaigns spanning multiple earth observing platforms incorporating balloons, mesosphere-stratosphere-troposphere radars, and rockets. Therefore, a mobile whole atmosphere lidar that implements such a field-widened MZI receiver would address this critical need of routinely profiling the wind and temperature through the atmosphere column. Such lidar ability would help discover the source(s) of the thermospheric gravity waves and the short-period inertia gravity waves recently observed in Antarctica [6,15,16], and would help address many other scientific issues [2–5,12,17] from a single, mobile ground platform.

Liu and Kobayashi [18] were the first to propose the use of a Mach–Zehnder interferometer as a frequency discriminator for direct-detection Doppler lidar. Their proposed transmitter used the Nd:YAG fundamental (1.064 μm) and inferred wind predominantly from aerosol, rather than molecular, scattering. Bruneau [19] optimized their MZI for pure molecular scattering and demonstrated wind measurements extending to 40 km [20]. Our approach, which is based on the latter configuration, is the first optimized for use with a resonance-fluorescence Doppler lidar to make use of both molecular scattering and resonance fluorescence simultaneously. Since the MZI configured for molecular scattering is capable of resolving a Doppler shift from both the aerosol and molecular contributions, all altitudes are accessible. Furthermore, the shorter optical path difference of an MZI optimized for molecular scattering versus an MZI optimized for aerosol scattering allows more extensive field widening [21]. Field widening is crucial for resonance lidars since they require a large transmitter beam divergence to avoid the saturation of the metal layers in combination with large collecting areas to detect weak returns from the upper atmospheres [10]. Accommodating these field widths would be impractical for the Fabry–Perot interferometers used in edge techniques [22–24].

In addition, unlike atomic filters, which provide spectral sensitivity at the price of discarding a portion of the spectrum of the received signal, interferometers serve only to sort the light into separate detection channels. Therefore, provided that the detection sensitivity in each channel is equal or known, recovery of the original signal can be accomplished by simply adding, or scaling and adding, the contributions from each channel. In this way, wind and temperature can be derived from the MLT region and temperature from the Rayleigh signal region simultaneously alongside the Rayleigh Doppler wind measurement without compromising the measurement precision. This property represents an advantage over the Na double-edge magneto-optic filter [25,26] and other atomic or molecular absorption-based filtering methods. The field-widened Mach–Zehnder is particularly well suited to Fe Doppler lidars since atomic absorption filters employing Fe would need to operate at a prohibitively high temperature.

## 2. RESONANCE DOPPLER AND MACH–ZEHNDER MEASUREMENT CONCEPTS

### A. Measurement Principles of Resonance Doppler Lidars

The Fe Doppler lidar is one of a class of lidars referred to as resonance-fluorescence Doppler or "resonance Doppler" lidars, which exploit the exceptionally high absorption and backscatter cross sections of metals deposited by meteor ablation in the MLT region, typically Fe, Na, or K, to sense wind and temperature in this region [13]. By probing the backscatter cross section at three fixed frequencies distributed about the resonance absorption line peak, these lidars infer the Doppler broadening and bulk Doppler shift of the line by the relative backscatter strength, thereby making a measurement of the temperature and wind of the backscatter volume, respectively [13]. This three-frequency technique was first applied to the narrow-band Na and K Doppler lidars [27–31], and has only recently been applied to the narrow-band Fe Doppler lidars [32,33]. Laser technology at the time limited the first Fe lidars to broad-band systems that were capable only of temperature measurements using the Fe Boltzmann and Rayleigh integration

techniques [34–36]. Recent developments have introduced narrow-band laser systems capable of measuring wind also, the Major Research Instrumentation (MRI) Fe Doppler lidar in Boulder, Colorado [33,10] being the first example of three-frequency Fe Doppler lidar. This lidar is capable of measuring temperature and wind in the MLT region and temperatures below the metal layers down to 30 km with a transmitter locked to the Fe transition of $a^5D_4 - z^5F_5^0$ at 372 nm and shifted alternately in time by 742 MHz above and below the transition wavelength [32,33]. Its reliance on the spectroscopy of Fe restricts the routine wind measurement range to regions of persistent Fe (typically 75–120+ km). Therefore, to measure wind below this range would require a spectrally sensitive receiver, such as the one that will be described in the next section. In addition to the three-frequency Doppler technique, a scanning Doppler technique has been applied to Na Doppler at 589 nm [37], K Doppler at 770 nm [38], and Fe Doppler lidar at 386 nm [39,40], which probes many frequencies through the Doppler broadened spectrum [41].

### B. Description of Rayleigh–Mie Doppler Techniques

Non-resonance direct-detection techniques are methods by which the Doppler shift of light is converted to a change in signal strength on a detector surface or set of pixels on a detector array by a high-resolution optical filter in the lidar receiver. A variety of optical filters have been investigated for suitability in such Rayleigh–Mie Doppler lidars, including interferometers such as the Fabry–Perot [22–24,42,43], the Fizeau [44], and the Mach–Zehnder [18–20], both in on-axis and fringe-imaging configurations [45], and atomic filters, such as the sodium double-edge magneto-optical filter [25,26] and the iodine vapor filter [46–49]. Measurement accuracies of most direct-detection methods are susceptible to variations in the aerosol backscatter ratio, temperature, and/or pressure of the backscatter volume [46,50]. Fringe-imaging techniques avoid this problem by imaging the complete spectrum, but at the expense of reduced collection and detection efficiency and increased complexity [51]. The double-edge Fabry–Perot method partially resolved this issue by locating two Fabry–Perot fringes symmetrically about the laser line [23,24], but the compensation for variations in temperature and aerosol backscatter ratio can only be perfect for a zero Doppler shift. The concept of a Mach–Zehnder as a spectral discriminator for lidar was introduced later on [18], with the advantage that by essentially measuring the phase, rather than the amplitude, of the interferometer's response, the Doppler shift could be retrieved directly, independent of any symmetrical broadening exhibited by the source's spectrum. Two schemes were proposed using the Mach–Zehnder: the dual Mach–Zehnder or "DMZ," which used just one optical path difference to estimate the phase (Fig. 1), and the quad Mach–Zehnder or "QMZ," which used, principally, a polarization-multiplexed interferometer comprising two optical path differences with a fixed $\pi/2$ optical phase difference between them (Fig. 2). We review these two measurement techniques in Section 2.C.

### C. Comparison of DMZ and QMZ Methods

As derived in Appendices A and B, for a light source with an arbitrary but symmetrical spectrum, the equations relating the signal of the DMZ to a Doppler frequency shift $\nu$ are

$$S_1 = \eta_1 P[1 + M_a M_1 \sin(2\pi\nu/\mathrm{FSR})]$$
$$S_2 = \eta_2 P[1 - M_a M_2 \sin(2\pi\nu/\mathrm{FSR})], \quad (1)$$

where FSR is the equivalent free spectral range of the MZI, $P$ is the total input power of the light source, $\eta_{1,2}$ are the products of the optical and detector efficiencies for channels 1 and 2, respectively, $M_a$ is a contrast factor that depends on the light source spectral broadening from the atmosphere, and $M_{1,2}$ are contrast factors that depend on instrument imperfections, as shown in Appendices A and B. Appendix B shows the important result that convolution with arbitrary but symmetrical input spectra only results in a contrast ($M_a$) reduction, not a change in the apparent phase of the instrument response. If the detection efficiencies are assumed equal and the instrument imperfections are ignored (i.e., $\eta_1 = \eta_2 = \eta_{\mathrm{Det}}/2$ and $M_{1,2} = 1$), the discrimination signal can be written as

$$Q_{\mathrm{DMZ}} = \frac{S_1 - S_2}{S_1 + S_2} = M_a \sin(2\pi\nu/\mathrm{FSR}). \quad (2)$$

Note that the measured discrimination signal of DMZ is a function not only of the Doppler shift, but of the spectral

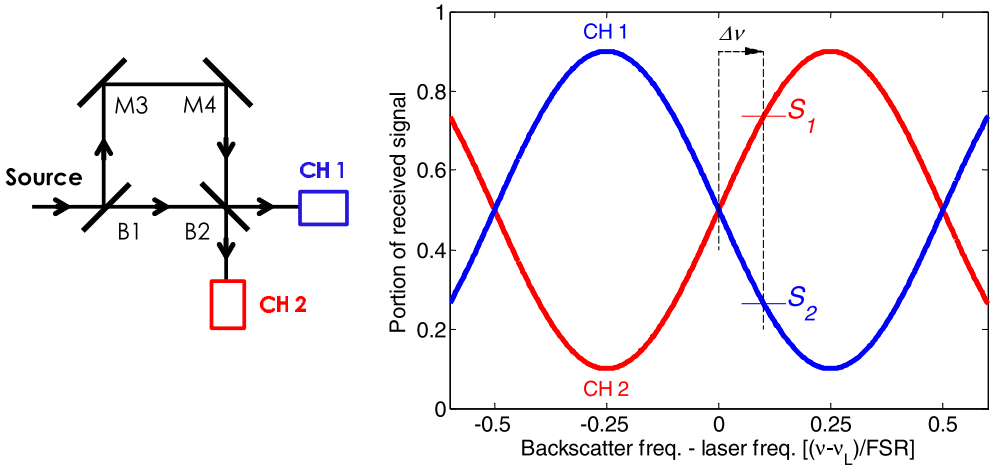


**Fig. 1.** Illustration of the dual Mach–Zehnder (DMZ) arrangement and spectral response curves. It is assumed that the optical path-length difference and laser frequency coincide with the cross-point shown. Estimating the phase of the spectral response requires assumptions about the amplitude of the response, which is a function of the source spectrum and instrument imperfections.

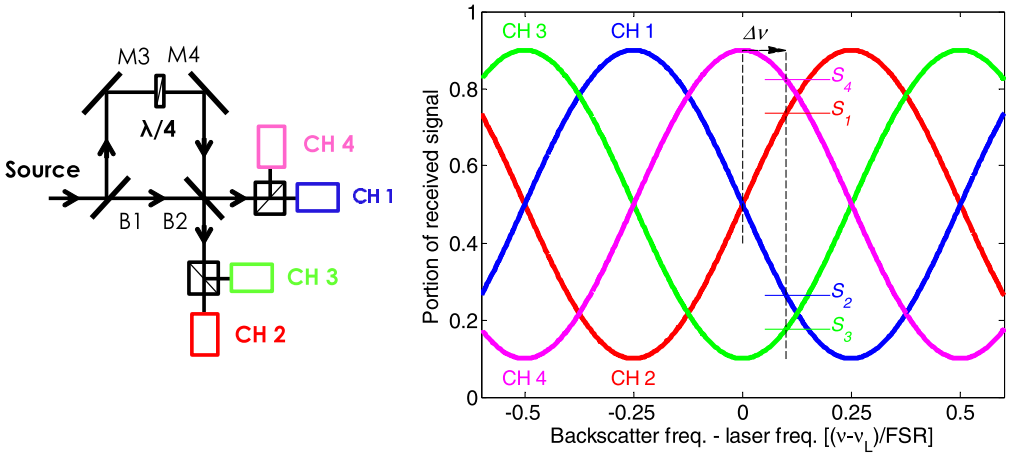


**Fig. 2.** Illustration of the quad Mach–Zehnder (QMZ) arrangement and spectral response curves. The QMZ is a polarization-multiplexed Mach–Zehnder with a quarter-waveplate that introduces a retardation to the slow-axis polarization. With four independent measurements, the phase of the spectral response can be measured independently of the source spectrum.

broadening via $M_a$ as well, which is a function of unknowns such as the aerosol backscatter ratio, temperature, pressure, and turbulence of the lidar detection volume. This problem is overcome by the QMZ, which uses a polarization-multiplexed MZI. The equations relating the four signals of the QMZ to a unit Doppler shift are

$$\begin{aligned} S_1 &= \eta_1 P[1 + M_a M_1 \sin(2\pi\nu/\mathrm{FSR})] \\ S_2 &= \eta_2 P[1 - M_a M_2 \sin(2\pi\nu/\mathrm{FSR})] \\ S_3 &= \eta_3 P[1 + M_a M_3 \cos(2\pi\nu/\mathrm{FSR})] \\ S_4 &= \eta_4 P[1 - M_a M_4 \cos(2\pi\nu/\mathrm{FSR})]. \end{aligned} \quad \textbf{(3)}$$

Equation (3) is valid for a light source with an arbitrary but symmetrical spectrum and geometric ray. If the detector efficiencies are again assumed equal, and the instrument imperfections are ignored (i.e., $\eta_{1,2,3,4} = \eta_{\mathrm{Det}}/4$ and $M_{1,2,3,4} = 1$), we can write the following discrimination signal from the four channels of signals:

$$\begin{aligned} Q_{\mathrm{QMZ}} &= \left(\frac{S_1 - S_2}{S_1 + S_2}\right)\left(\frac{S_3 - S_4}{S_3 + S_4}\right)^{-1} = \frac{M_a \sin(2\pi\nu/\mathrm{FSR})}{M_a \cos(2\pi\nu/\mathrm{FSR})} \\ &= \tan(2\pi\nu/\mathrm{FSR}). \end{aligned} \quad \textbf{(4)}$$

Equation (4) indicates that this QMZ measurement is independent of all but the bulk Doppler shift itself—the quantity of interest. However, the backscattered power is distributed among four signals, two of which possess no sensitivity to the Doppler shift (see Fig. 2), resulting in a factor of $\sqrt{2}$ less precision for the QMZ versus the DMZ method in which the power is distributed between only two signals, both of which are maximally sensitive to the Doppler shift.

A later work presented the Mach–Zehnder interferometer for molecular scattering analysis [19,20] using a smaller optical path differences (3–5 cm) and lower spectral resolution. Although less sensitive to a unit Doppler shift than the aerosol implementation [18], the ability to resolve Doppler shifts from molecules as well as aerosols makes this technique especially well suited to contiguous profiling through the troposphere, stratosphere, and lower mesosphere. This same work [19] also found the performance of the DMZ to be superior to that of the Fabry–Perot method in low background conditions, which was experimentally confirmed in [20].

In summary, the Mach–Zehnder techniques offer certain advantages over other Rayleigh Doppler techniques. The DMZ, for example, offers a simpler optical arrangement with lower optical quality requirements than the Fabry–Perot, and can use basic, single anode photomultipliers as detectors. The ability to recover all of the backscattered power is an advantage over atomic vapor filters. However, by making the MZI insensitive to the aerosol backscatter ratio and other broadening mechanisms by way of the QMZ technique, its precision is degraded. In Section 2.D, we present a technique that offers a less severe performance tradeoff between the DMZ and QMZ techniques while preserving the QMZ's insensitivity to the backscatter spectrum.

### D. Multi-Phase Mach–Zehnder "XMZ" Approach and Integration With a Resonance Doppler Lidar

In this work, we analyze a field-widened DMZ interferometer for the task of combining, using the same resonance Fe Doppler beam, Rayleigh–Mie Doppler lidar measurements from the troposphere to mesosphere with resonance Doppler measurements that extend upwards from the mesosphere to the extended lower thermosphere. The concept is then to marry a Rayleigh–Mie Doppler direct-detection lidar technique with the resonance Doppler lidar technique to cover wind measurements throughout the whole atmosphere. Rather than operating at a single transmitted frequency, we investigate the benefits of using the three available transmitted frequencies of this resonance Doppler lidar system in combination with the DMZ system. We will refer to this scheme as the multi-phase ("X") Mach–Zehnder or "XMZ," since, in principle, an arbitrary number of spectral response phases/frequencies is possible in this scheme. We will show that by using the information from three frequencies (Fig. 3), a Doppler shift estimate can be made independent of not only the atmospheric contrast factor, but also the instrument contrast factors when the return lidar signal is a symmetrical function in the spectrum.

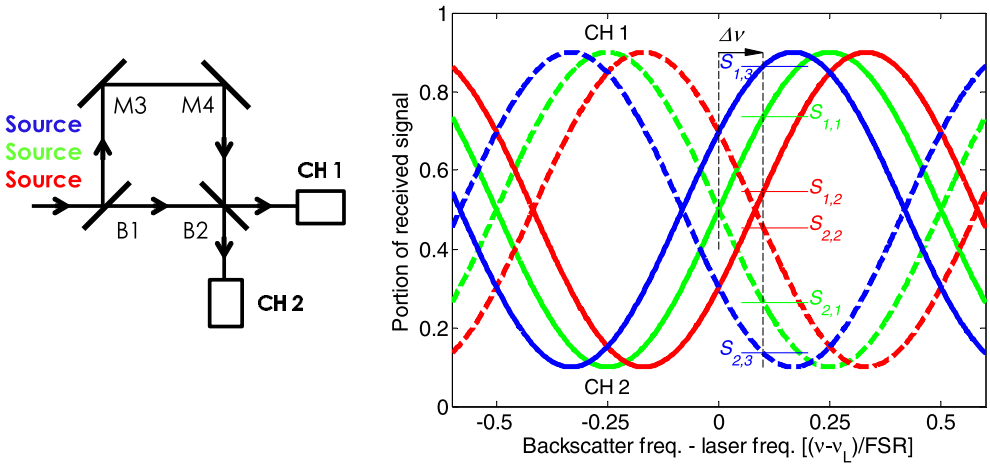


**Fig. 3.** Illustration of the multi-phase Mach–Zehnder (XMZ) arrangement and spectral response curves. (a) Each frequency is represented by a different color. (b) Each frequency "sees" the corresponding instrument response function. By multiplexing the source's central frequency, rather than the optical path difference, the XMZ technique can be made insensitive to broadening and aerosol influences on the source backscatter spectrum.

Consider the DMZ signals for three transmitted frequencies:

$$\begin{aligned}[S_{1,2}]_0 &= \eta_{1,2}P_0[1 \pm M_a M_{1,2}\ \sin(2\pi\nu/\mathrm{FSR})]\\ [S_{1,2}]_{-\phi} &= \eta_{1,2}P_-[1 \pm M_a M_{1,2}\ \sin(2\pi(\nu - f_\Delta)/\mathrm{FSR})]\\ [S_{1,2}]_{+\phi} &= \eta_{1,2}P_+[1 \pm M_a M_{1,2}\ \sin(2\pi(\nu + f_\Delta)/\mathrm{FSR})],\end{aligned} \quad \textbf{(5)}$$

where $f_\Delta$ is the amount of shift in the frequency of the transmitter and subscripts 0, $-\phi$, and $+\phi$ indicate properties pertaining to the center, red-shifted, and blue-shifted transmitted frequencies, respectively. We assume that the atmospheric contrast factor $M_a$ does not change significantly between the switching of each transmitter frequency and that the ratio of the detector efficiencies ($\eta_1/\eta_2 \to \beta$) is known from the calibration, which is described in Section 3.C. Once again, we define the discrimination signals, $Q_\Phi$, for each set of channels $[S_{1,2}]_\Phi$. Here, the phase $\Phi$ is 0, $-\phi$, or $+\phi$. With the following substitutions, $(M_1 + M_2)M_a \to m_1$ and $(M_1 - M_2)M_a \to m_2$, we arrive at

$$\begin{aligned}Q_0 &= \frac{[S_1]_0 - \beta[S_2]_0}{[S_1]_0 + \beta[S_2]_0} = \frac{m_1 \sin(2\pi\nu/\mathrm{FSR})}{2 + m_2 \sin(2\pi\nu/\mathrm{FSR})}\\ Q_{-\phi} &= \frac{[S_1]_{-\phi} - \beta[S_2]_{-\phi}}{[S_1]_{-\phi} + \beta[S_2]_{-\phi}} = \frac{m_1 \sin(2\pi(\nu - f_\Delta)/\mathrm{FSR})}{2 + m_2 \sin(2\pi(\nu - f_\Delta)/\mathrm{FSR})}\\ Q_{+\phi} &= \frac{[S_1]_{+\phi} - \beta[S_2]_{+\phi}}{[S_1]_{+\phi} + \beta[S_2]_{+\phi}} = \frac{m_1 \sin(2\pi(\nu + f_\Delta)/\mathrm{FSR})}{2 + m_2 \sin(2\pi(\nu + f_\Delta)/\mathrm{FSR})}.\end{aligned} \quad \textbf{(6)}$$

Note that of the variables present in the three independent equations of Eq. (6), only the factors $m_1$, $m_2$, and the Doppler shift $\nu$ are unknowns. We can therefore solve for the three unknowns and obtain a measurement of the Doppler shift from the Rayleigh and Mie scattering signals with an accuracy that is free of the influence of the atmospheric contrast and instrument contrast factors. The benefits of the XMZ technique are possible due to a reduction in the number of variables compared to the QMZ technique described in Section 2.B, which required a waveplate, two polarizers, and two additional detectors, each with associated uncertainties.

Another key benefit of the Mach–Zehnder techniques, including the XMZ technique described above, is that all of the signal is recovered and the summation of both signals $S_1$ and $S_2$ results in a quantity free of interference effects, provided the balance of $\eta_1 M_1 = \eta_2 M_2$ is reached or the ratio is known, as shown in Eq. (7).

$$\begin{aligned}S_1 &= f(\nu_C) \otimes \eta_1 P[1 + M_1 \cos(2\pi\nu_C/\mathrm{FSR})]\\ S_2 &= f(\nu_C) \otimes \eta_2 P[1 - M_2 \cos(2\pi\nu_C/\mathrm{FSR})]\\ &\text{If } \eta_1 M_1 = \eta_2 M_2,\\ S_1 + S_2 &= f(\nu_C) \otimes \left\{ \begin{matrix} \eta_1 P[1 + M_1 \cos(2\pi\nu_C/\mathrm{FSR})] \\ +\eta_2 P[1 - M_2 \cos(2\pi\nu_C/\mathrm{FSR})] \end{matrix} \right\}\\ &= f(\nu_C) \otimes P[\eta_1 + \eta_2 + (\eta_1 M_1 - \eta_2 M_2)\\ &\quad \times \cos(2\pi\nu_C/\mathrm{FSR})]\\ S_1 + S_2 &= f(\nu_C) \otimes (\eta_1 + \eta_2)P = (\eta_1 + \eta_2)P\\ &\quad \left( \int_{-\infty}^{+\infty} f(\nu' - \nu_C)\mathrm{d}\nu' = 1 \right)\\ &\text{If the ratio } \eta_1 M_1/\eta_2 M_2 \text{ is known,}\\ S_1 + S_2 \cdot \frac{\eta_1 M_1}{\eta_2 M_2} &= f(\nu_C) \otimes \left\{ \begin{matrix} \eta_1 P[1 + M_1 \cos(2\pi\nu_C/\mathrm{FSR})] \\ +\eta_1 \frac{M_1}{M_2} P[1 - M_2 \cos(2\pi\nu_C/\mathrm{FSR})] \end{matrix} \right\}\\ &= f(\nu_C) \otimes P\left[\eta_1 + \eta_1 \frac{M_1}{M_2} + (\eta_1 M_1 - \eta_1 M_1)\right.\\ &\quad \left. \times \cos(2\pi\nu_C/\mathrm{FSR})\right]\\ S_1 + S_2 \cdot \frac{\eta_1 M_1}{\eta_2 M_2} &= f(\nu_C) \otimes \left[\eta_1 + \eta_1 \frac{M_1}{M_2}\right] P = \left[1 + \frac{M_1}{M_2}\right] \eta_1 P.\end{aligned}$$

**(7a)**

Note that Eq. (7a) is obtained for any arbitrary spectrum distribution of the light source with a centroid frequency $\nu_c$, including the backscatter spectrum of the resonance fluorescence, which is not, in general, symmetrical. Equation (7)

has a significant meaning because, after summation or scaling and summation, the original resonance fluorescence and Rayleigh scattering signals $P$ can be recovered with a proportional factor $\eta_1+\eta_2$ or $\eta_1(1+M_1/M_2)$. As they are constant and the same for all three transmitted frequencies, such proportional factors are cancelled out when taking the temperature ratio $R_T$ and wind ratio $R_W$ to derive the temperature and radial wind in the MLT region using the three-frequency ratio technique [13]. For example, one set of the metric ratios can be defined as

$$R_T=\frac{[S_{1+2}]_{+\phi}+[S_{1+2}]_{-\phi}}{[S_{1+2}]_0}=\frac{P_{+\phi}+P_{-\phi}}{P_0}$$
$$R_W=\frac{[S_{1+2}]_{+\phi}-[S_{1+2}]_{-\phi}}{[S_{1+2}]_0}=\frac{P_{+\phi}-P_{-\phi}}{P_0}, \tag{7b}$$

where $S_{1+2}$ is the summation or scaling and summation of signals $S_1$ and $S_2$ as defined in Eq. (7). The metric ratios obtained in Eq. (7b) are exactly the same as the original ones if the Mach–Zehnder interferometer is not in the receiver path, meaning that, after summation or scaling and summation, the same resonance Doppler lidar techniques for retrieving the wind and temperature in the MLT region described in Section 2.A are still valid, provided that the balance of $\eta_1M_1=\eta_2M_2$ is reached or the ratio is known. Unlike techniques that discard a portion of the return spectrum [26,52], the MZI techniques preserve the input, thereby permitting the retrieval of the wind and temperature in the MLT region by the usual three-frequency technique [13] and with very nearly the original precision. Consequently, the Fe Doppler lidar techniques [13,32,33] will be used above ~75 km to derive wind and temperature from Fe resonance fluorescence, while the XMZ-based Rayleigh–Mie Doppler technique will be applied below the Fe layers.

## 3. DESIGN AND IMPLEMENTATION OF XMZ

Having settled on the XMZ concept as the Rayleigh–Mie Doppler variety of choice to extend wind measurements below the mesopause region, we now address design specifics, including the choice of this instrument's free spectral range, the optical layout and field widening scheme, and the detector balancing and path-length stabilization methods. Our main design goal is to choose a free spectral range (FSR) that minimizes the wind measurement uncertainty for a typical lidar backscatter spectrum. The desired optical path-length difference (OPD) determined by this FSR is then achieved in a tilted optical layout. Another design goal is to widen the XMZ's field of view for suitability with resonance Doppler lidar.

### A. Selecting a Free Spectral Range for Maximum Molecular Sensitivity

The goal of choosing an optimum FSR is to maximize the sensitivity of a single-phase discrimination signal $Q_\Phi$ to a unit Doppler shift. Following the analysis by [19], the contrast of the MZI response determines the sensitivity and is largely a function of the backscatter spectral width. If we assume that the backscatter is purely from low-pressure molecular scattering, where the thermal broadening mechanism dominates, the discrimination signal for the central, unshifted channel can be modeled. The pure thermal broadening gives a Gaussian spectrum

$$f(\nu'-\nu_c)=\frac{1}{\sqrt{\pi}\sigma_D}\exp\left[-\frac{(\nu'-\nu_c)^2}{\sigma_D^2}\right],$$
$$\sigma_D=\frac{2}{\lambda}\sqrt{\frac{2k_BT}{m}}, \tag{8}$$

where $\sigma_D$ is the $1/e$ half-width of the backscatter spectrum for the Rayleigh scattering, $\nu_c$ is the central frequency, $k_B$ is the Boltzmann constant, $T$ is the atmosphere temperature, $m$ is the mean mass of the air molecules, and $\lambda$ is the laser wavelength. For such a Gaussian light source, the atmospheric contrast factor is also a Gaussian given by the Fourier transform $M_a=F(t)=\Im\{f(\nu_c)\}$ at $t=1/\mathrm{FSR}$ (see Appendix B). If instrument imperfections are again ignored ($\eta_1=\eta_2$ and $M_1=M_2$), we obtain the same discrimination signal as given by Eq. (2). Substituting $M_a$, we have

$$Q=\frac{S_1-S_2}{S_1+S_2}=M_a\sin\left(\frac{2\pi\nu}{\mathrm{FSR}}\right)$$
$$=\exp\left(-\pi^2\left(\frac{\sigma_D}{\mathrm{FSR}}\right)^2\right)\sin\left(\frac{2\pi\nu}{\mathrm{FSR}}\right), \tag{9}$$

where $\mathrm{FSR}=c/\mathrm{OPD}$ is determined by the OPD. We can then find a value of OPD that maximizes the sensitivity of the discrimination signal to a unit Doppler shift. This sensitivity is given by:

$$\frac{\partial Q_0}{\partial\nu}=\frac{2\pi}{\mathrm{FSR}}\exp\left(-\pi^2\left(\frac{\sigma_D}{\mathrm{FSR}}\right)^2\right)\cos\left(\frac{2\pi\nu}{\mathrm{FSR}}\right). \tag{10}$$

By taking $\frac{\partial(\partial Q/\partial\nu)}{\partial\mathrm{FSR}}=0$ about the zero Doppler shift point, $\nu=0$, the sensitivity in Eq. (10) is maximized for

$$\mathrm{FSR}=\pi\sqrt{2}\sigma_D\approx 4.44\sigma_D. \tag{11}$$

For a wavelength of 372 nm and a temperature of 250 K, the optimal free spectral range is then 9 GHz, corresponding to an optimal OPD of 33.1 mm. The optimal OPD varies from 38.0 to 31.3 mm for 190–280 K at zero line of sight (LOS) wind, and varies from 33.1 to 30.6 mm for LOS winds from 0 to 107 m/s at 250 K (see Fig. 4). The choices of 250 K and its corresponding OPD of 33.1 mm are representative, but not critical. Slight deviations about 33.1 mm are acceptable because the sensitivity changes by no more than 3% for an error in the FSR of 5 mm, as shown in Fig. 4.

### B. Field Widening and Optical Arrangement of Tilted Mach–Zehnder

To give the Mach–Zehnder sufficient fringe contrast for a resonance lidar receiver, its angular field must be wide enough to accommodate a beam divergence that is large enough to avoid saturation in the metal layer for a telescope with a collecting area of 0.5 $m^2$ or more. That is, the optical path-length difference between the two legs of the interferometer must remain constant to within a fraction of a wavelength over the range of input angles defined by the optical extent, or étendue, of the telescope receiver and the clear aperture of the interferometer's optics. Mertz [53] found that the field of an MZI could be widened by several orders of magnitude by inserting a refractive slab into one leg of the interferometer. We follow the procedure of Hilliard and Shepherd [21] to compute the optimum slab thickness for a tilted Mach–Zehnder of an arbitrary incident

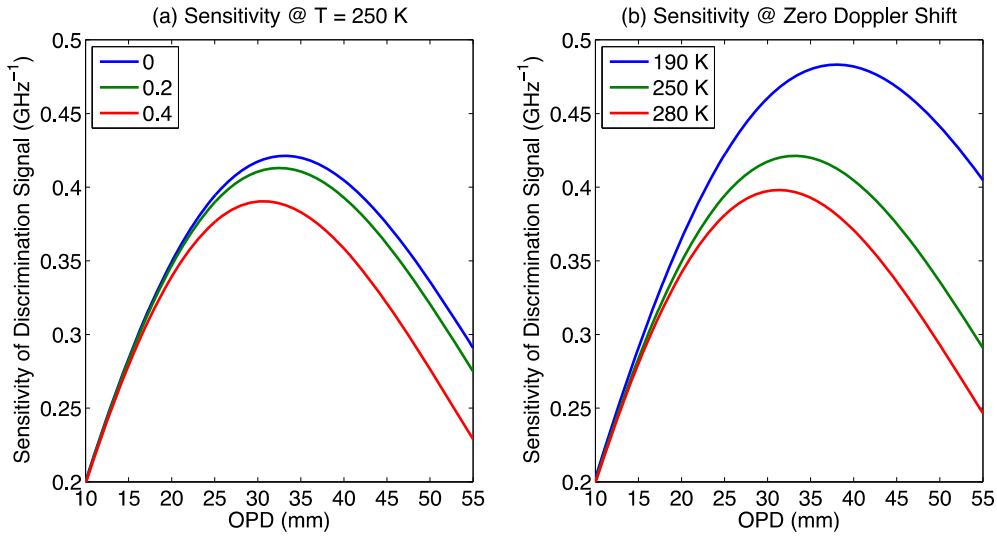


**Fig. 4.** Sensitivity of discrimination signal to a unit Doppler shift $\partial Q_0/\partial \nu$ versus the OPD is given for different line-of-sight winds and temperatures. (a) At temperature of 250 K, the sensitivity is computed for the normalized LOS winds of 0, 0.2, and 0.4 (blue, green, and red), which correspond to the LOS winds of 0, 53.6, and 107.2 m/s. (b) At a zero Doppler shift, the sensitivity is computed for temperatures of 190, 250, and 280 K (blue, green, and red).

tilt angle $\theta$, that is, for an optical arrangement in which the interferometer is a near-parallelogram with optics at each vertex and acute angles of approximately $2\theta$ (Fig. 5).

The desired OPD, termed as the quasi-zero path difference (QZP) in [21], for a slab tilted at an incident angle $\theta$ can be found from the geometry in Fig. 6(a). For a particular incident angle, in this case equal to the incident tilt angle $\theta$, a thickness $t'$ can be defined such that the slab's refracted ray and the image ray are collinear. This condition exists when Eq. (12) is satisfied, wherein a subscripted $n$ denotes a refracted angle:

$$t \tan \theta_n = t' \tan \theta. \tag{12}$$

Using Snell's law to determine $\theta_n$, we relate $t'$ to the thickness $t$, index $n$ of the slab, and the incident tilt angle $\theta$

$$t' = \frac{t}{n} \frac{\cos \theta}{\sqrt{1 - \sin^2 \theta / n^2}}. \tag{13}$$

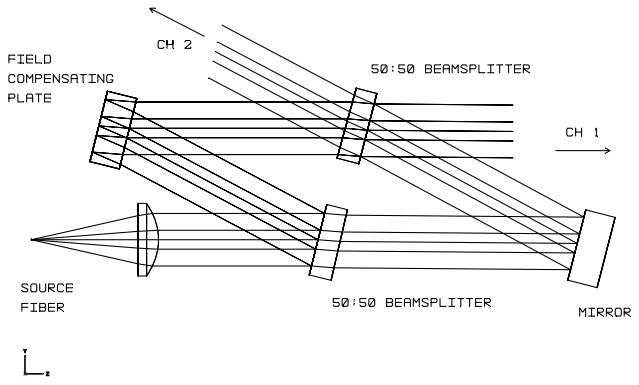


**Fig. 5.** Illustration of tilted Mach–Zehnder from a ZEMAX model. In this configuration, the compensating plate is a second-surface mirror with a thickness of approximately 20.86 mm. Each surface is tilted by 14°.

The quasi-zero path difference QZP is now

$$\begin{aligned} \mathrm{QZP} &= 2na - 2b = 2n\left(\frac{t}{\cos \theta_n}\right) - 2\left(\frac{t'}{\cos \theta}\right) \\ &= \frac{2(n^2 - 1)t}{\sqrt{n^2 - \sin^2 \theta}}. \end{aligned} \tag{14}$$

Note that for a tilt angle of zero, the solution reduces to $2(nt - t/n)$, which is the result obtained for a slab at normal incidence [21]. Following the same procedure, a more general geometry is illustrated, wherein the incident angle is no longer exactly $\theta$, but deviated by some small angle $\Delta\phi$ representing a ray from an off-axis field [Fig. 6(b)]. In this geometry, the actual OPD becomes

$$\begin{aligned} \mathrm{OPD} &= 2na - 2b - s \\ &= 2t\left(\sqrt{n^2 - \sin^2(\theta + \Delta\phi)} - \frac{\cos\theta \cos(\theta + \Delta\phi)}{\sqrt{n^2 - \sin^2 \theta}}\right) \end{aligned}$$

$$\mathrm{OPD} - \mathrm{QZP} \approx t \frac{(n^2 - 1)\sin^2 \theta}{(n^2 - \sin^2 \theta)^{3/2}} \Delta\phi^2 + O(\Delta\phi^3). \tag{15}$$

The difference OPD–QZP shows a measure of the quality of field compensation. For a non-zero slab incident angle, the difference between the actual OPD and the desired QZP exhibits a $\Delta\phi^2$ dependence on the field angle rather than $\Delta\phi^4$, as was found for a slab used at normal incidence [21]. Nevertheless, the compensation for a 14° tilt angle and a 33.13 mm optical path difference is still adequate for sufficiently small fields. For example, a typical resonance Doppler lidar telescope with a 500 μrad field of view and an 800 mm aperture will result in a field that is compensated to $\lambda/24$ at 372 nm over a 35 mm pupil. The half-angle of light entering the interferometer is equal to the half-angle of the telescope field of view scaled by the ratio of the useful aperture of the telescope to that of the interferometer. Smaller tilt angles will provide better field compensation and less sensitivity to

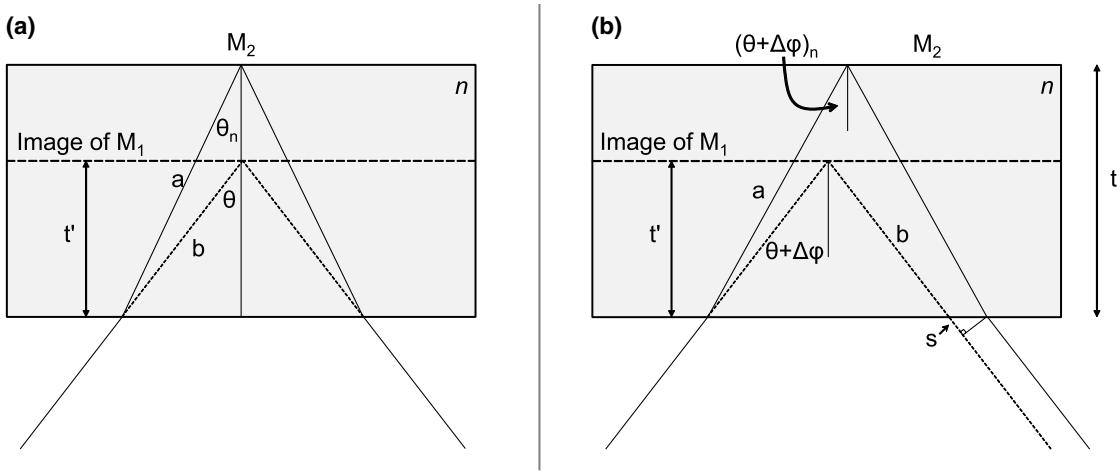


**Fig. 6.** Illustration of the condition for (a) the quasi-zero path difference and (b) for angles deviated from $\theta$, so the optical path difference becomes $2na - 2b - s$.

polarization, but are difficult to accommodate in a compact optical layout.

### C. Stabilization of the Interferometer and Detector Balancing

The optical path difference of the MZI is susceptible to temperature and pressure fluctuations and, in this scheme, must be continually stabilized to a reference source to remove variations in the outputs that may be misinterpreted as a Doppler shift. In some systems, reference light is provided by injecting a small portion of the transmitter pulse into the receiver (e.g., [24,54]). This is an effective method in analog detection systems, wherein the pulse energy can be measured reliably. Photon-counting detection systems cannot be used with pulsed reference light due to the pulse pileup phenomenon in photomultipliers (PMTs) and a quenching dead time in Geiger-mode avalanche photodiodes (APDs). Most data acquisition systems in resonance lidar employ photon-counting detection only, therefore precluding the use of the reference pulse technique. Instead, one viable method is to inject a square pulse of CW light into the telescope timed to coincide with the end of each shot (Fig. 7). The CW source will faithfully represent the central frequency of the pulsed source provided that the chirp is compensated for, which is accomplished in the Fe Doppler lidar by optical heterodyne detection [55]. To modulate the CW beam, a pair of acousto-optic modulators (AOMs) are oriented so that

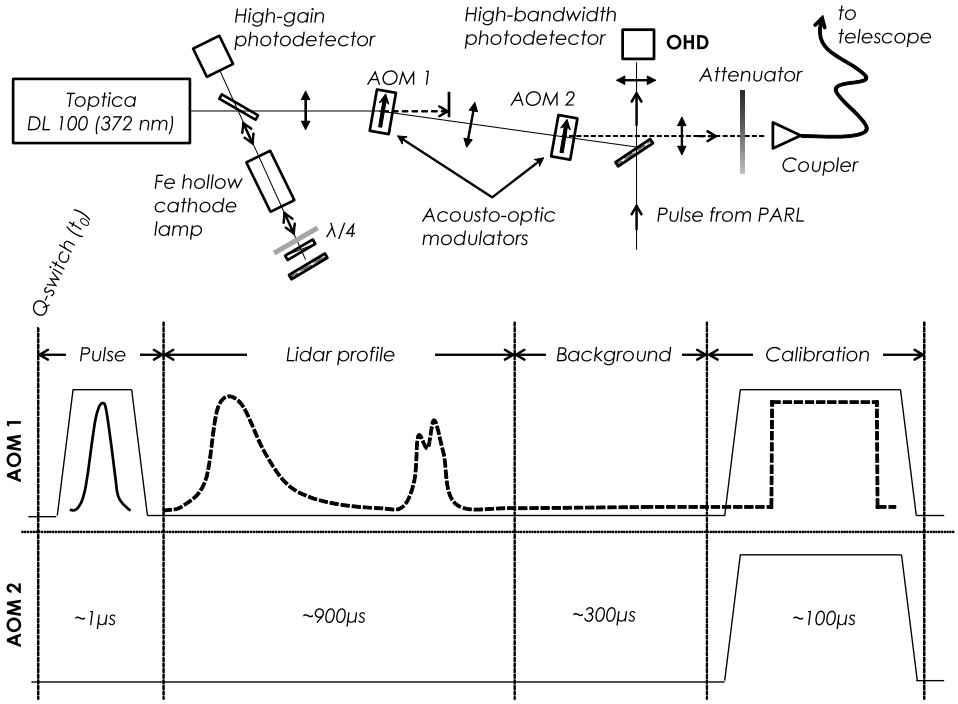


**Fig. 7.** Illustration of the method by which the laser is locked and light is rapidly modulated on and off to expose the MZI receiver, for a brief period, to narrow-band light that is closely representative of the central frequency of laser pulses.

the latter AOM compensates for the frequency shift imposed by the first. In this way, the AOMs together function as a high-speed shutter (~100 ns rise/fall time), and allow exposing a precisely timed pulse of the zero wind reference at a specific delay after each shot. After a set number of shot accumulations, a discrimination signal is computed from the accumulated zero wind reference light and a correction to a leg of the MZI is made by tuning a piezo-actuated stage or to the Doppler bias in post-processing. Provided the drift is slow compared to the shot accumulation period, this method of compensation should be sufficient.

Any detector sensitivity imbalance will also introduce a wind bias and must be compensated for. Since background light levels are usually much higher than the detector dark count rate, even at night, the background light could be used to measure the imbalance. Alternatively, an incoherent source, such as a light-emitting diode (LED), could be periodically blinked into the telescope to create a reference. Since the output of both the LED and background would be spectrally broad compared to the free spectral range of the MZI, no fringes would be observed and the light would be equally split between both channels, allowing the apparent LED or background signal level from the detectors to reveal their relative sensitivity. Consider Eq. (1), and replace $P$ with the received power from a broadband source such as an LED or background light. For such a broadband source, $M_a \to 0$ (see Appendix B), and Eq. (1) becomes

$$\begin{aligned} S_1 &= \eta_1 P \\ S_2 &= \eta_2 P \\ \beta &= S_1/S_2 = \eta_1/\eta_2. \end{aligned} \tag{16}$$

Note that $\eta_1$ and $\eta_2$ include both optical and detector efficiencies, so $\beta$ includes the effects of both the optical and detector imbalances.

## 4. PERFORMANCE ANALYSIS AND INITIAL RESULTS

### A. Comparison of Theoretical Performances of DMZ, QMZ, and XMZ

A treatment of the theory of the measurement of the Doppler shift using the DMZ and QMZ techniques is provided in Bruneau [19]. If the detection efficiencies are assumed equal and instrument imperfections are ignored, discriminator signals for the XMZ and QMZ configurations can be defined that are insensitive to the temperature, aerosol, and pressure variations of the lidar detection volume. The XMZ and QMZ configurations are therefore our preferred methods for the retrieval of wind in the stratosphere and upper troposphere. One advantage of the XMZ configuration is that since all three frequencies ($f_0$, $f_0 - f_\Delta$, $f_0 + f_\Delta$) and associated discriminator signals are sensitive to the Doppler shift, one can then define a discriminator signal that yields a measurement performance similar to the DMZ, but, unlike the DMZ, is insensitive to backscatter spectrum. The shot-noise-limited performances of the XMZ, DMZ, and QMZ techniques are compared here (see Appendix C for derivations of XMZ).

For comparison with the DMZ and QMZ techniques analyzed in Bruneau [19], we introduce the discriminator signals with a normalized wind speed $u'$, wherein the following substitution is made and the optimum free spectral range given by Eq. (11) for the chosen reference temperature $T_0$ is used.

$$\begin{aligned} 2\pi\frac{\nu}{\mathrm{FSR}} &\to u' \\ u' &= 2\pi\frac{2u/\lambda}{\pi\sqrt{2}\sigma_D} = \left(\frac{kT_0}{m}\right)^{-1/2} u, \end{aligned} \tag{17}$$

where $\nu = 2u/\lambda$ is the Doppler frequency shift induced by the LOS wind $u$. Under ideal conditions, whereby detection efficiencies are assumed equal and instrument imperfections are ignored ($\beta = 1$ and $m_2 = 0$), with this substitution, the discriminator signals for the DMZ, QMZ, and XMZ become

$$\begin{aligned} Q_{\mathrm{DMZ}} &= \frac{\sin u'}{\sqrt{e}} \\ Q_{\mathrm{QMZ}} &= \tan u' \\ Q_{\mathrm{XMZ}} &= \frac{\sin(u'-\phi) + \sin u' + \sin(u'+\phi)}{\sin(u'-\phi) - \sin(u'+\phi)} \\ &= -\frac{1+2\cos\phi}{2\sin\phi}\tan u' \\ \phi &= f_\Delta\left(\frac{2}{\lambda}\sqrt{\frac{kT_0}{m}}\right)^{-1} = 2\pi f_\Delta/\mathrm{FSR}. \end{aligned} \tag{18}$$

The frequency of the AOM shift $f_\Delta$ is 742 MHz. The reference temperature $T_0$ is 250 K, and the wavelength $\lambda$ is 372 nm. Thus, the phase shift determined by the operation conditions of the base Fe Doppler lidar is $\phi \approx 0.515$. The measurement performances of all three techniques are given here, with the performance for the DMZ and QMZ techniques given by Bruneau [19] in Eq. (19). $\Delta Q$ is the square root of the variance of $Q$. Performance is measured as the shot-noise-limited wind speed error, which is the product of the uncertainty in the discriminator signal $\Delta Q$ and the inverse of its sensitivity $(\partial Q/\partial u')^{-1}$. At $u' = 0$,

$$\begin{aligned} \Delta u'_{\mathrm{QMZ}} &= \Delta Q \cdot \left(\frac{\partial Q}{\partial u'}\right)^{-1} \sim \frac{2.33}{\sqrt{\sum_i S_i}} \\ \Delta u'_{\mathrm{DMZ}} &\sim \frac{1.65}{\sqrt{\sum_i S_i}} \\ \Delta u'_{\mathrm{XMZ}} &\sim \frac{1.75}{\sqrt{\sum_i S_i}}, \end{aligned} \tag{19}$$

where $\sum_i S_i$ is the sum total of the photon counts in all frequencies and channels. The XMZ possesses a measurement performance that is 25% better than the QMZ for an AOM shift of 742 MHz while preserving the QMZ's key feature, which is insensitivity to aerosol, temperature, and pressure effects. Equation (20) (see its derivation in Appendix C) gives the relationship of wind error versus the choice of phase (i.e., the AOM shift frequency) for XMZ at $u' = 0$:

$$\Delta u'_{\mathrm{XMZ}} = \sqrt{\frac{3}{4N}\left(\frac{3e}{\sin^2\phi} - 2\right)} \cdot \left(\frac{1+2\cos\phi}{2\sin\phi}\right)^{-1}. \tag{20}$$

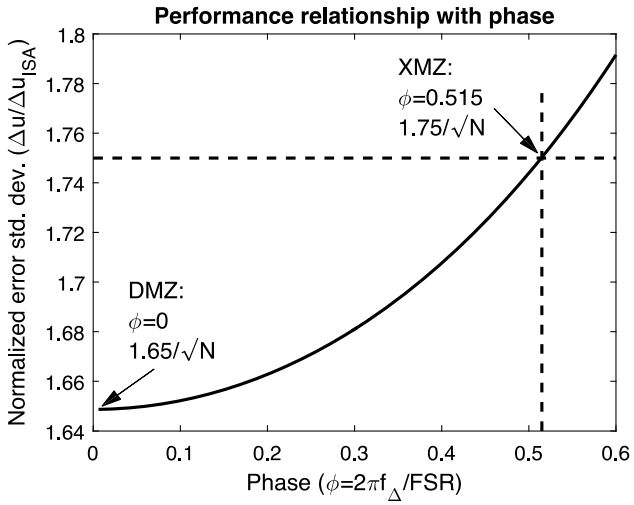


**Fig. 8.** ISA-normalized radial wind uncertainty of XMZ measurements is given as a function of the phase shift induced by the AOM shift.

As plotted in Fig. 8, the LOS wind error for XMZ reaches the minimum, i.e., the limit of DMZ, when the phase (frequency) shift is approaching zero. This is understandable because XMZ becomes DMZ if the frequency shift is zero. The AOM shift of 742 MHz, determined by the optimization of the base Fe Doppler lidar [33], turns out to be a reasonable choice for XMZ. Further increase of the AOM shift will increase the wind error of XMZ.

It is of great interest to compare XMZ with QMZ and DMZ on the ideal spectrum analyzer (ISA)-normalized standard deviation of the wind-velocity measurement error as a function of the normalized wind velocity [19]. Appendix C provides the derivation for XMZ, and the results are illustrated in Fig. 9. Up to the maximum geophysical radial wind speeds in the region of interest (~50 m/s), the uncertainty of XMZ wind measurements increases by no more than 10% from the zero Doppler point.

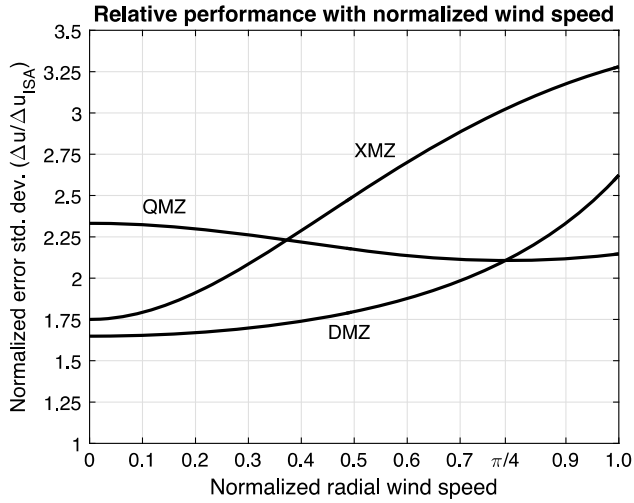


**Fig. 9.** ISA-normalized standard deviation of the wind-velocity measurement error is given as a function of the normalized wind velocity for XMZ, QMZ, and DMZ. The AOM shift used for XMZ is 742 MHz, corresponding to a phase shift of ~0.515.

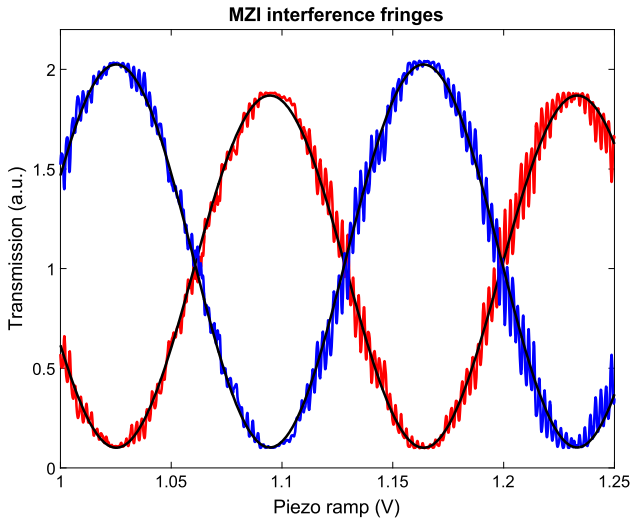


**Fig. 10.** Fringes obtained by scanning a leg of the interferometer with a piezo stage. The source has an optical extent equivalent to that of the actual receiver fiber. A second-surface mirror of 20.86 mm thickness in one leg serves as the field compensating plate. The instrumental contrast factors for both channels are approximately 0.90 in this figure.

### B. Present and Expected Results

Field widening using the compensating plate has been demonstrated, and an instrument-limited fringe contrast ($M_{1,2}$) of between 0.89 and 0.93 has been obtained with the apparatus (Fig. 10). One leg of the interferometer is varied by ramping a piezo-actuated stage to view the interference. The mirror, beam splitters, and field compensating plate were polished and coated by LightMachinery to obtain transmitted and reflected wavefront errors of better than lambda/30. The actual optical path-length difference of the XMZ is measured to be 33.62 mm. A fiber with a core diameter of 1000 μm and an NA of 0.22 was filled on the input side with light from a narrow linewidth, Toptica 372 nm DL-100 external cavity diode laser. Illumination from this fiber provided the range of angles representing the optical extent of the true receiver source. Frequencies matching the resonant acoustic modes of the enclosure were evident in the scans from insufficient damping of ambient acoustic noise, but the long-term drift is small due to the thermally compensated design.

Based on data obtained from the Fe Doppler lidar to date, we have plotted the expected wind uncertainty (Fig. 11). This figure includes data that was taken with the transmitter operating at a reduced power level of 1.45 W due to optical damage concerns. An upgrade to the optics will allow the lidar to operate at power levels of up to ~6 W. Once the design power is attained, the wind measurement precision will be within 4 m/s for a 15 minute and 3 km resolution up to 75 km, above which the wind measurement is accomplished from the resonance three-frequency technique. For the present power levels, we still expect a precision of 1 m/s up to 50 km and a maximum uncertainty of 8 m/s at 76 km at a resolution of 15 minutes horizontally and 2.9 km vertically. The parameters of the lidar transmitter and receiver are listed in Table 1. It is worth pointing out that the base Fe Doppler lidar is currently running in a

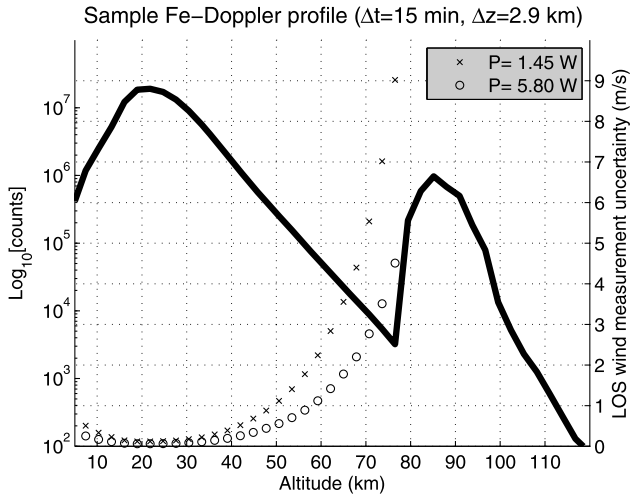


**Fig. 11.** Accumulation of lidar profiles from the Fe Doppler lidar taken around midnight local time on October 20, 2014 is plotted here to show the expected radial wind uncertainty. The transmitter power was 1.45 W. The sudden enhancement above 75 km is due to resonant scattering from Fe in the mesopause region, where the three-frequency technique takes over for wind and temperature.

**Table 1. Parameters of the Fe Doppler Lidar Transmitter and Receiver**

| | |
|---|---|
| **Transmitter Parameters** | |
| Power | 1.45 W (~6 W planned) |
| Wavelength in vacuum | 372.0995 nm |
| Pulse spectral width | 35–55 MHz (chirp-limited) |
| Pulse repetition rate | 35 Hz |
| Pulse temporal width | 250 ns (FWHM) |
| Full angle beam divergence | 250 μrad |
| **Receiver parameters** | |
| Field of view | 500 μrad |
| Collecting area | 0.5 $m^2$ |
| PMT QE | 43% |

monostatic, biaxial arrangement to prevent the near-field returns from saturating the photo detector. To extend XMZ wind measurements to near ground, dual analog/photon-counting detection can be employed to resolve the dynamic range issues. In addition, a second receiver could be used to collect the near-field returns.

## 5. CONCLUSIONS

We have described a method of extending the wind measurement range of an Fe Doppler lidar from the MLT region down to the surface or near surface using a tilted, field-widened, multi-phase Mach–Zehnder interferometer (XMZ). By detecting the signal at both channels of the interferometer, and at three distinct frequencies within a quarter of the free spectral range, the wind measurement accuracy can be made free of the influence of the aerosol backscatter ratio, temperature, and Brillouin scattering contributions to the backscatter spectrum. In addition, the uncertainty of the measurement is limited to only 1.75 times the Cramer–Rao lower bound, and there are only two detectors to balance. Provided that the detection sensitivity in each channel is known, the original resonance fluorescence and Rayleigh scattering signals can be recovered by simply scaling and adding the contributions from both channels. Consequently, the wind and temperature can be derived from the MLT region and temperature from the Rayleigh region simultaneously alongside Rayleigh Doppler wind measurement with the same receiver without compromising the measurement precision. The impact that an imbalance in the detector sensitivities will have on the winds and temperatures measured by the three-frequency technique in the MLT region will be the focus of a future work.

Fluctuations in aerosol backscatter ratio can affect the measurement if the AOM up- and down-shifted frequencies are not alternated quickly enough. Since the pulse repetition rate of the laser is 35 Hz, aerosols would not have an impact on the measurement provided that the timescale for change in the aerosol backscatter ratio is greater than 3 inter-pulse periods, or approximately 90 ms. The accumulation of pulses will further reduce the statistical variance of the Doppler shift sensitivity to aerosols. The temperature and pressure are less variable in the stratosphere and upper troposphere and have less of an effect on the sensitivity than aerosols in the lower atmosphere. Furthermore, by measuring the instrument and atmospheric contrast factors along with the Doppler shift, as presented in Eq. (6), the sensitivity to a unit Doppler shift is measured in addition to the wind with the XMZ technique. Consequently, the change in sensitivity caused by variations in atmospheric parameters, though impacting the measurement uncertainty, will not affect the wind measurement accuracy. Therefore, implementing the XMZ technique in a three-frequency mobile Fe Doppler lidar has the potential to address the critical need for profiling the wind and temperature through the atmospheric column. Wind and temperature profiling below the MLT region represents a key step toward achieving the goal of a whole atmosphere lidar for pursuing compelling new frontiers in atmospheric and space sciences.

## APPENDIX A: INSTRUMENT RESPONSE OF MZI WITH OPTICAL IMPERFECTIONS

If reflection/transmission ratios of two beam splitters that differ from 50:50 are assumed, we have the following Eq. (A1) for the electric fields on photodetectors 1 and 2 in DMZ. This assumes a perfectly monochromatic source, i.e., single-frequency light, with radial frequency $\omega$, wavenumber $k$, and arbitrary initial phase $\phi_o$, and this light source has ideal collimation with zero beam divergence, i.e., the geometry ray.

$$\begin{aligned}\tilde{E}_1(t) &= E_0\sqrt{T_1}\sqrt{T_2}\,\exp(i(\omega t + kd_1 + \phi_0)) \\ &\quad + E_0\sqrt{R_1}\sqrt{R_3}\sqrt{R_4}\sqrt{R_2}\,\exp(i(\omega t + kd_2 + \phi_0)) \\ \tilde{E}_2(t) &= E_0\sqrt{T_1}\sqrt{R_2}\,\exp(i(\omega t + kd_1 + \phi_0 + \pi)) \\ &\quad + E_0\sqrt{R_1}\sqrt{R_3}\sqrt{R_4}\sqrt{T_2}\,\exp(i(\omega t + kd_2 + \phi_0)),\end{aligned} \tag{A1}$$

where $E_0$ is the electric field amplitude of the light source, $R_{1,2}$ and $T_{1,2}$ are the reflectivity and transmission of their respective beam splitters, $R_{3,4}$ are the reflectivity of two high-reflection

mirrors, $t$ is time, and $d_1$ and $d_2$ are the optical path lengths of legs 1 and 2, respectively. Note that the reflectivity and transmission are defined as the ratios of the absolute reflected and transmitted power over the total input power. Considering the loss of two beam splitters, $A_{1,2}$, caused by scattering and absorption, we have $R_{1,2} + T_{1,2} = 1 - A_{1,2}$. The power/intensity incident on detectors 1 and 2 is then given by Eq. (A2):

$$P_1(k) = P_0\eta_{\mathrm{Opt},1}[1 + M_{\mathrm{Opt},1}\cos(k(d_1 - d_2))]$$
$$P_2(k) = P_0\eta_{\mathrm{Opt},2}[1 - M_{\mathrm{Opt},2}\cos(k(d_1 - d_2))], \quad \textbf{(A2)}$$

where $P_0 \propto E_o^2$ is the total input power of the light source, and

$$\eta_{\mathrm{Opt},1} = T_1T_2 + R_1R_2R_3R_4$$
$$M_{\mathrm{Opt},1} = \frac{2\sqrt{T_1T_2R_1R_2R_3R_4}}{T_1T_2 + R_1R_2R_3R_4}$$
$$\eta_{\mathrm{Opt},2} = T_1R_2 + R_1T_2R_3R_4$$
$$M_{\mathrm{Opt},2} = \frac{2\sqrt{T_1T_2R_1R_2R_3R_4}}{T_1R_2 + R_1T_2R_3R_4}. \quad \textbf{(A3)}$$

If the beam splitter loss due to absorption and scattering is zero ($A = 0$), $R_{1,2} = T_{1,2} = 1/2$, and $R_{3,4} = 1$, then we have $\eta_{\mathrm{Opt},1} = \eta_{\mathrm{Opt},2} = 1/2$ and $M_{\mathrm{Opt},1} = M_{\mathrm{Opt},2} = 1$. Consequently, Eq. (A2) reduces to the familiar expressions for two-beam interference under ideal conditions [Eq. (A4)]:

$$P_1(k) = \frac{P_0}{2}[1 + \cos(k(d_1 - d_2))]$$
$$P_2(k) = \frac{P_0}{2}[1 - \cos(k(d_1 - d_2))]. \quad \textbf{(A4)}$$

The signal from the detector, or "instrument response function," is $S = \eta_{\mathrm{Det}}P$, where $\eta_{\mathrm{Det}}$ is an efficiency that includes the detector efficiency and losses that occur between the interferometer and the detector. Including these efficiencies, we have for the instrument response functions of each channel:

$$S_1(k) = \eta_{\mathrm{Opt},1}\eta_{\mathrm{Det},1}P_0[1 + M_{\mathrm{Opt},1}\cos(k(d_1 - d_2))]$$
$$S_2(k) = \eta_{\mathrm{Opt},2}\eta_{\mathrm{Det},2}P_0[1 - M_{\mathrm{Opt},2}\cos(k(d_1 - d_2))]. \quad \textbf{(A5)}$$

Substituting $k = 2\pi/\lambda = 2\pi\nu_c/c$ into Eq. (A5), we obtain

$$S_1(\nu_C) = \eta_{\mathrm{Opt},1}\eta_{\mathrm{Det},1}P_0[1 + M_{\mathrm{Opt},1}\cos(2\pi\nu_C/\mathrm{FSR})]$$
$$S_2(\nu_C) = \eta_{\mathrm{Opt},2}\eta_{\mathrm{Det},2}P_0[1 - M_{\mathrm{Opt},2}\cos(2\pi\nu_C/\mathrm{FSR})], \quad \textbf{(A6)}$$

where $\mathrm{FSR} = c/|d_1 - d_2|$ is the equivalent free spectral range, $\lambda$ is the wavelength, and $c$ is the speed of light. The central frequency of the light source, $\nu_c$, is determined by the transmitted laser frequency $\nu_L$ and Doppler shift $\nu$ as $\nu_c = \nu_L - \nu$. The FSR can be finely tuned by adjusting the optical path-length difference $(d_1 - d_2)$ within the range of a laser wavelength $\lambda$ to make

$$2\pi\nu_c/\mathrm{FSR} = \frac{2\pi\nu_L}{\mathrm{FSR}} - \frac{2\pi\nu}{\mathrm{FSR}} = 2\pi q + \frac{\pi}{2} - \frac{2\pi\nu}{\mathrm{FSR}}, \quad \textbf{(A7)}$$

where $q$ is an integer number. Therefore, we can change the cosine in Eq. (A6) to a sine:

$$S_1(\nu) = \eta_{\mathrm{Opt},1}\eta_{\mathrm{Det},1}P_0[1 + M_{\mathrm{Opt},1}\sin(2\pi\nu/\mathrm{FSR})]$$
$$S_2(\nu) = \eta_{\mathrm{Opt},2}\eta_{\mathrm{Det},2}P_0[1 - M_{\mathrm{Opt},2}\sin(2\pi\nu/\mathrm{FSR})]. \quad \textbf{(A8)}$$

Note that the Doppler frequency shift $\nu = 2u/\lambda$ is determined by the line-of-sight wind $u$. Appendix B will introduce the case where the source is not monochromatic, but has an arbitrary but symmetrical spectrum.

## APPENDIX B: CONVOLUTION OF MZI RESPONSE WITH ARBITRARY SOURCE SPECTRUM

For a source with a normalized spectral distribution $f(\nu_C)$, the received signal in each channel is the incoherent superposition of the intensity patterns produced by multiple frequencies, i.e., a convolution between this distribution and the instrument response function [Eq. (A6)]:

$$S_1(\nu_C) = f(\nu_C) \otimes \eta_{\mathrm{Opt},1}\eta_{\mathrm{Det},1}P_0\lfloor 1 + M_{\mathrm{Opt},1}\cos(2\pi\nu_C/\mathrm{FSR})\rfloor, \quad \textbf{(B1)}$$

where $\nu_c$ is the centroid frequency of the distribution that is equal to the central frequency for a symmetrical spectrum. Considering that function $f(\nu)$ is normalized to 1, simplification yields

$$\begin{aligned} S_1(\nu_C) &= \eta_{\mathrm{Opt},1}\eta_{\mathrm{Det},1}P_0[f(\nu_C) \otimes 1 \\ &\quad + f(\nu_C) \otimes M_{\mathrm{Opt},1}\cos(2\pi\nu_C/\mathrm{FSR})] \\ &= \eta_{\mathrm{Opt},1}\eta_{\mathrm{Det},1}P_0[1 + M_{\mathrm{Opt},1}f(\nu_C) \\ &\quad \otimes \cos(2\pi\nu_C/\mathrm{FSR})]. \end{aligned} \quad \textbf{(B2)}$$

In the Fourier domain, defining $\Im\{f(\nu_C)\} = F(t)$, we obtain

$$\begin{aligned} &f(\nu_C) \otimes \cos(2\pi\nu_C/\mathrm{FSR}) \\ &= \Im^{-1}\{\Im\{f(\nu_C)\} \cdot \Im\{\cos(2\pi\nu_C/\mathrm{FSR})\}\} \\ &= \Im^{-1}\left\{F(t) \cdot \frac{1}{2}\left[\delta\left(t - \frac{1}{\mathrm{FSR}}\right) + \delta\left(t + \frac{1}{\mathrm{FSR}}\right)\right]\right\} \\ &= \frac{1}{2}\left(\Im^{-1}\left\{F(t)\delta\left(t - \frac{1}{\mathrm{FSR}}\right)\right\}\right. \\ &\quad \left. + \Im^{-1}\left\{F(t)\delta\left(t + \frac{1}{\mathrm{FSR}}\right)\right\}\right). \end{aligned} \quad \textbf{(B3)}$$

Using the properties of the Dirac delta function and inverse Fourier transform, we can write

$$\begin{aligned} &f(\nu_C) \otimes \cos(2\pi\nu_C/\mathrm{FSR}) \\ &= \frac{1}{2}\left[F\left(\frac{1}{\mathrm{FSR}}\right)\exp\left(-\frac{i2\pi\nu_C}{\mathrm{FSR}}\right)\right. \\ &\quad \left. + F\left(-\frac{1}{\mathrm{FSR}}\right)\exp\left(+\frac{i2\pi\nu_C}{\mathrm{FSR}}\right)\right]. \end{aligned} \quad \textbf{(B4)}$$

If the backscatter spectrum is symmetrical about $\nu_c$ and $f(\nu' - \nu_c) = f(\nu_c - \nu')$, then $f(\nu_C)$ is an even function centered about $\nu_C = 0$. Consequently, $F(t)$ is also even and we can write

$$f(\nu_C) \otimes \cos(2\pi\nu_C/\mathrm{FSR}) = F(1/\mathrm{FSR})\frac{1}{2}\left[\exp\left(-\frac{i2\pi\nu_C}{\mathrm{FSR}}\right) + \exp\left(+\frac{i2\pi\nu_C}{\mathrm{FSR}}\right)\right] = F(1/\mathrm{FSR})\cos(2\pi\nu_C/\mathrm{FSR}). \quad \textbf{(B5)}$$

Therefore, for a source with an even functioned spectral distribution, we have

$$S_1(\nu_C) = \eta_{\mathrm{Opt},1}\eta_{\mathrm{Det},1}P_0[1 + M_{\mathrm{Opt},1}M_a\cos(2\pi\nu_C/\mathrm{FSR})]$$
$$M_a = F(1/\mathrm{FSR})$$
$$F(t) = \Im\{f(\nu_C)\}. \quad \textbf{(B6)}$$

The only change to the instrument function is a reduction in the contrast with, critically, no change to the phase. The same could be shown for channel $S_2$. For convenience, we will combine the optical and detector efficiencies into a single factor (i.e., $\eta_{\mathrm{Opt},x}\eta_{\mathrm{Det},x} \to \eta_x$) and replace $M_{\mathrm{Opt},x}$ with $M_x$ throughout the text. Making the same notation of $\nu_c = \nu_L - \nu$ and FSR tuning as in Appendix A, the cosine in Eq. (B6) can be changed to a sine. Therefore, we obtain

$$S_1(\nu) = \eta_1 P_0[1 + M_1 M_a \sin(2\pi\nu/\mathrm{FSR})]$$
$$S_2(\nu) = \eta_2 P_0[1 - M_2 M_a \sin(2\pi\nu/\mathrm{FSR})]. \quad \textbf{(B7)}$$

## APPENDIX C: THEORETICAL PERFORMANCE OF XMZ

We wish to know the uncertainty in the Doppler frequency shift estimate, which is the product of the uncertainty in the discrimination signal and the inverse of the sensitivity of the discrimination signal to a unit Doppler shift. Here, we make the substitutions $2\pi\nu/\mathrm{FSR} \to u'$ and $2\pi f_\Delta/\mathrm{FSR} \to \phi$, and treat the Doppler shift as a phase shift along the spectral response of the MZI.

$$\Delta u_{\mathrm{XMZ}} = \frac{\partial u}{\partial Q}\cdot\Delta Q = \Delta Q\cdot\left(\frac{\partial Q}{\partial u}\right)^{-1}$$
$$Q = \frac{Q_{-\phi} + Q_0 + Q_{+\phi}}{Q_{-\phi} - Q_{+\phi}}, \quad \textbf{(C1)}$$

where $Q_0$, $Q_{-\phi}$, and $Q_{+\phi}$ are the discrimination signals for the central, red-shifted, and blue-shifted frequencies (phases), respectively. To simplify the analysis, we assume the ideal condition that the detection efficiencies are equal and that instrument imperfections are ignored; therefore, $\eta_1 = \eta_2 = \eta_{\mathrm{Det}}/2$ and $M_1 = M_2 = 1$ in Eq. (5), and $\beta = 1$, $m_1 = 2M_a$, and $m_2 = 0$ in Eq. (6), which define $Q_0$, $Q_{-\phi}$, and $Q_{+\phi}$. Each frequency's discrimination signal is a ratio of the difference of the signals of the two MZI channels to their sum. In the general case of a Gaussian spectrum, at the reference temperature and with the optimum FSR given by Eq. (11), the signals in each channel for each frequency or phase are given by:

$$S_{1,\Phi} = \frac{N}{6}\left[1 + \frac{1}{\sqrt{e}}\sin(u' + \Phi)\right]$$
$$S_{2,\Phi} = \frac{N}{6}\left[1 - \frac{1}{\sqrt{e}}\sin(u' + \Phi)\right]$$
$$Q_\Phi = \frac{S_{1,\Phi} - S_{2,\Phi}}{S_{1,\Phi} + S_{2,\Phi}} = \frac{1}{\sqrt{e}}\sin(u' + \Phi), \quad \textbf{(C2)}$$

where the phase $\Phi$ is either 0, $-\phi$, or $+\phi$, depending on the transmitted frequency, and $N$ is the sum total number of signal counts in all three frequencies at a given range interval $N = \sum_i S_i$. Here, we assume that an equal amount of signal is present at each frequency. We then define a ratio of the discrimination signals of all three phases that is insensitive to the backscatter spectral width:

$$Q = \frac{Q_{-\phi} + Q_0 + Q_{+\phi}}{Q_{-\phi} - Q_{+\phi}} = \frac{\sin(u' - \phi) + \sin u' + \sin(u' + \phi)}{\sin(u' - \phi) - \sin(u' + \phi)} = -\frac{1 + 2\cos\phi}{2\sin\phi}\tan u'. \quad \textbf{(C3)}$$

With Eq. (C3), we can then define the sensitivity of the discriminator signal to a unit Doppler shift about an arbitrary Doppler shift:

$$\frac{\partial Q}{\partial u'} = -\frac{1 + 2\cos\phi}{2\sin\phi}\cdot\frac{1}{\cos^2 u'}. \quad \textbf{(C4)}$$

The uncertainty in the discriminator signal $\Delta Q$ can be estimated by a first-order approximation of the errors contributed by each signal $S_1$ and $S_2$ for each of the three phases as

$$\Delta Q = \sqrt{\overline{\left[\sum_{n,\Phi}\left(\frac{\partial Q}{\partial S_{n,\Phi}}\Delta S_{n,\Phi}\right)\right]^2}} = \sqrt{\sum_{n,\Phi}\left(\frac{\partial Q}{\partial S_{n,\Phi}}\right)^2 \mathrm{var}(S_{n,\Phi})}. \quad \textbf{(C5)}$$

The variance of the signals for each channel and frequency, assuming a negligible background, are

$$\mathrm{var}(S_{1,0}) = \frac{N}{6}\left(1 + \frac{1}{\sqrt{e}}\sin u'\right)$$
$$\mathrm{var}(S_{2,0}) = \frac{N}{6}\left(1 - \frac{1}{\sqrt{e}}\sin u'\right)$$
$$\mathrm{var}(S_{1,-\phi}) = \frac{N}{6}\left(1 + \frac{1}{\sqrt{e}}\sin(u' - \phi)\right)$$
$$\mathrm{var}(S_{2,-\phi}) = \frac{N}{6}\left(1 - \frac{1}{\sqrt{e}}\sin(u' - \phi)\right)$$
$$\mathrm{var}(S_{1,+\phi}) = \frac{N}{6}\left(1 + \frac{1}{\sqrt{e}}\sin(u' + \phi)\right)$$
$$\mathrm{var}(S_{2,+\phi}) = \frac{N}{6}\left(1 - \frac{1}{\sqrt{e}}\sin(u' + \phi)\right). \quad \textbf{(C6a)}$$

At $u = u' = 0$, the variances are simplified to

$$\mathrm{var}(S_{1,0}) = \mathrm{var}(S_{2,0}) = \frac{N}{6}$$
$$\mathrm{var}(S_{1,-\phi}) = \mathrm{var}(S_{2,+\phi}) = \frac{N}{6}\left(1 - \frac{1}{\sqrt{e}}\sin\phi\right)$$
$$\mathrm{var}(S_{1,+\phi}) = \mathrm{var}(S_{2,-\phi}) = \frac{N}{6}\left(1 + \frac{1}{\sqrt{e}}\sin\phi\right). \quad \textbf{(C6b)}$$

The sensitivity of the discrimination signal to each individual signal, i.e., the error coefficient, is

$$\frac{\partial Q}{\partial S_{1,0}} = \frac{3}{N}\cdot\frac{\sqrt{e}-\sin u'}{\sin(u'-\phi)-\sin(u'+\phi)}$$
$$\frac{\partial Q}{\partial S_{2,0}} = -\frac{3}{N}\cdot\frac{\sqrt{e}+\sin u'}{\sin(u'-\phi)-\sin(u'+\phi)}$$
$$\frac{\partial Q}{\partial S_{1,-\phi}} = -\frac{\sin(u')+2\sin(u'+\phi)}{[\sin(u'-\phi)-\sin(u'+\phi)]^2}\cdot\frac{3}{N}\left[\sqrt{e}-\sin(u'-\phi)\right]$$
$$\frac{\partial Q}{\partial S_{2,-\phi}} = \frac{\sin(u')+2\sin(u'+\phi)}{[\sin(u'-\phi)-\sin(u'+\phi)]^2}\cdot\frac{3}{N}\left[\sqrt{e}+\sin(u'-\phi)\right]$$
$$\frac{\partial Q}{\partial S_{1,+\phi}} = \frac{\sin(u')+2\sin(u'-\phi)}{[\sin(u'-\phi)-\sin(u'+\phi)]^2}\cdot\frac{3}{N}\left[\sqrt{e}-\sin(u'+\phi)\right]$$
$$\frac{\partial Q}{\partial S_{2,+\phi}} = -\frac{\sin(u')+2\sin(u'-\phi)}{[\sin(u'-\phi)-\sin(u'+\phi)]^2}\cdot\frac{3}{N}\left[\sqrt{e}+\sin(u'+\phi)\right]. \quad \textbf{(C7a)}$$

About the zero Doppler point, the error coefficients can be simplified to

$$\frac{\partial Q}{\partial S_{1,0}} = -\frac{3}{2N}\cdot\frac{\sqrt{e}}{\sin\phi}, \qquad \frac{\partial Q}{\partial S_{2,0}} = \frac{3}{2N}\cdot\frac{\sqrt{e}}{\sin\phi}$$
$$\frac{\partial Q}{\partial S_{1,-\phi}} = -\frac{3}{2N}\left[1+\frac{\sqrt{e}}{\sin\phi}\right], \qquad \frac{\partial Q}{\partial S_{2,-\phi}} = -\frac{3}{2N}\left[1-\frac{\sqrt{e}}{\sin\phi}\right]$$
$$\frac{\partial Q}{\partial S_{1,+\phi}} = \frac{3}{2N}\left[1-\frac{\sqrt{e}}{\sin\phi}\right], \qquad \frac{\partial Q}{\partial S_{2,+\phi}} = \frac{3}{2N}\left[1+\frac{\sqrt{e}}{\sin\phi}\right]. \quad \textbf{(C7b)}$$

Combining Eqs. (C6) and (C7) with Eq. (C5) yields the uncertainty in the discriminator signal $\Delta Q$ for an arbitrary Doppler shift and phase shift. For brevity, we assume from here on that the errors are calculated about the zero Doppler shift point.

$$\Delta Q = \sqrt{\sum_{n,\Phi}\left(\frac{\partial Q}{\partial S_{n,\Phi}}\right)^2 \mathrm{var}(S_{n,\Phi})} = \sqrt{\frac{3}{4N}(3e/\sin^2\phi - 2)}. \quad \textbf{(C8)}$$

This gives, for the uncertainty in the normalized wind speed for an ideal instrument,

$$\Delta u' = \Delta Q\cdot\left(\frac{\partial Q}{\partial u'}\right)^{-1} = \left(\frac{3}{4N}(3e/\sin^2\phi - 2)\right)^{1/2}\left(\frac{1}{2}(1+2\cos\phi)/\sin\phi\right)^{-1}$$
$$\phi = 2\pi f_{\mathrm{AOM}}/\mathrm{FSR} \approx 0.515$$
$$\Delta u' = 1.75/\sqrt{N}. \quad \textbf{(C9)}$$

For a reference temperature of 250 K, the line-of-sight wind speed error becomes

$$\Delta u = \Delta u'\left(\frac{kT_0}{m}\right)^{1/2} = \frac{469\ \mathrm{m/s}}{\sqrt{N}}. \quad \textbf{(C10)}$$

The values for the DMZ and QMZ have been presented in a previous work [19].

**Funding.** National Science Foundation (NSF) Major Research Instrumentation (AGS-0723229, AGS-1136272) National Aeronautics and Space Administration (NASA) Earth and Space Science Fellowship (NNX09AO35H); CIRES Innovative Research Program.

**Acknowledgment.** We sincerely acknowledge the support of the National Science Foundation (NSF) Major Research Instrumentation award AGS-0723229, a NASA Earth and Space Science Fellowship award (NNX09AO35H), and a CIRES Innovative Research Program award. John A. Smith sincerely acknowledges the generous support of the NASA Earth and Space Science Fellowship (NESSF) and of the CIRES Graduate Student Research Fellowship (GSRF). This work was also partially supported by an NSF grant.

## REFERENCES

1. X. Chu, "Advances in Middle Atmosphere Research with LIDAR," in *Proceeding of the 24th International Laser Radar Conference*, Boulder, Colorado (2008), pp. 769–772.
2. National Research Council, *Solar and Space Physics: A Science for a Technological Society*, The National Academies (2013).
3. R. R. Garcia, D. R. Marsh, D. E. Kinnison, B. A. Boville, and F. Sassi, "Simulation of secular trends in the middle atmosphere, 1950–2003," J. Geophys. Res **112**, D09301 (2007).
4. T. J. Fuller-Rowell, et al., "Impact of terrestrial weather on the upper atmosphere," Geophys. Res. Lett **35**, L09808 (2008).
5. R. A. Akmaev, "Whole atmosphere modeling: Connecting terrestrial and space weather," Rev. Geophys. **49**, RG4004 (2011).
6. X. Chu, Z. Yu, C. S. Gardner, C. Chen, and W. Fong, "Lidar observations of neutral Fe layers and fast gravity waves in the thermosphere (110–155 km) at McMurdo (77.8°S, 166.7°E), Antarctica," Geophys. Res. Lett. **38**, L23807 (2011).
7. X. Chu, Z. Yu, W. Fong, C. Chen, B. Roberts, W. Huang, X. Lu, T. Fuller-Rowell, C. Gardner, A. McDonald, and S. Vadas, "LIDAR observations of thermospheric Fe layers, temperatures and gravity waves at McMurdo, Antarctica," in *Coupling, Energetics and Dynamics of Atmospheric Regions (CEDAR) workshop*, Boulder, Colorado (2013).
8. J. S. Friedman, X. Chu, C. G. M. Brum, and X. Lu, "Observation of a thermospheric descending layer of neutral K over Arecibo," J. Atmos. Sol.-Terr. Phys. **104**, 253–259 (2013).
9. T. T. Tsuda, X. Chu, T. Nakamura, M. K. Ejiri, T. D. Kawahara, A. S. Yukimatu, and K. Hosokawa, "A thermospheric Na layer event observed up to 140 km over Syowa Station (69.0°S, 39.6°E) in Antarctica," Geophys. Res. Lett. **42**, 3647–3653 (2015).
10. J. A. Smith and X. Chu, "High-efficiency receiver architecture for resonance-fluorescence and Doppler lidars," Appl. Opt. **54**, 3173–3184 (2015).
11. Q. Gao, X. Chu, X. Xue, X. Dou, T. Chen, and J. Chen, "Lidar observations of thermospheric Na layers up to 170 km with a descending tidal phase at Lijiang (26.7ºN, 100.0ºE), China," J. Geophys. Res. Space Phys. **120**, 9213–9220 (2015).
12. OASIS, "Exploring the interaction of Earth's atmosphere with space," Report to National Science Foundation (NSF), 2014, available at http://rsss.csl.illinois.edu/workshop.
13. X. Chu and G. C. Papen, "Resonance fluorescence lidar for measurements of the middle and upper atmosphere," in *Laser Remote Sensing*, T. Fujii and T. Fukuchi, eds. (CRC Press, 2005), pp. 179–432.
14. A. Hauchecorne and M.-L. Chanin, "Density and temperature profiles obtained by lidar between 35 and 70 km," Geophys. Res. Lett. **7**, 565–568 (1980).
15. X. Chu, W. Huang, W. Fong, Z. Yu, Z. Wang, J. A. Smith, and C. S. Gardner, "First lidar observations of polar mesospheric clouds and Fe temperatures at McMurdo (77.8°S, 166.7°E), Antarctica," Geophys. Res. Lett. **38**, L16810 (2011).
16. C. Chen, X. Chu, A. McDonald, S. Vadas, Z. Yu, W. Fong, and X. Lu, "Inertia-gravity waves in Antarctica: A case study using simultaneous

lidar and radar measurements at McMurdo/Scott Base (77.8°S, 166.7°E)," J. Geophys. Res. Atmos. **118**, 2794–2808 (2013).
17. M. A. Geller, H.-L. Liu, J. H. Richter, D. Wu, and F. Zhang, "Gravity Waves in weather, climate, and atmospheric chemistry: issues and challenges for the community," in *Gravity Wave Retreat White Paper* (2006).
18. Z. Liu and T. Kobayashi, "Differential discrimination technique for incoherent Doppler lidar to measure atmospheric wind and backscatter ratio," Opt. Rev. **3**, 47–52 (1996).
19. D. Bruneau, "Mach-Zehnder interferometer as a spectral analyzer for molecular Doppler wind lidar," Appl. Opt. **40**, 391–399 (2001).
20. D. Bruneau, A. Garnier, A. Hertzog, and J. Porteneuve, "Wind-velocity lidar measurements by use of a Mach-Zehnder interferometer, comparison with a Fabry-Perot interferometer," Appl. Opt. **43**, 173–182 (2004).
21. R. Hilliard and G. Shepherd, "Wide-Angle Michelson Interferometer for Measuring Doppler Line Widths," J. Opt. Soc. Am. **56**, 362–369 (1966).
22. C. Korb, B. Gentry, and C. Weng, "Edge technique: theory and application to the lidar measurement of atmospheric wind," Appl. Opt. **31**, 4202–4213 (1992).
23. C. Flesia and C. Korb, "Theory of the double-edge molecular technique for Doppler lidar wind measurement," Appl. Opt. **38**, 432–440 (1999).
24. C. Flesia, C. Korb, and C. Hirt, "Double-edge molecular measurement of lidar wind profiles at 355 nm," Opt. Lett. **25**, 1466–1468 (2000).
25. W. Huang, X. Chu, B. Williams, S. Harrell, J. Wiig, and C.-Y. She, "Na double-edge magneto-optic filter for Na lidar profiling of wind and temperature in the lower atmosphere," Opt. Lett. **34**, 199–201 (2009).
26. W. Huang, X. Chu, J. Wiig, B. Tan, C. Yamashita, T. Yuan, J. Yue, S. Harrell, C.-Y. She, B. Williams, J. Friedman, and R. M. Hardesty, "Field demonstration of simultaneous wind and temperature measurements from 5 to 50 km with a Na double-edge magneto-optic filter in a multi-frequency Doppler lidar," Opt. Lett. **34**, 1552–1554 (2009).
27. K. S. Arnold and C. Y. She, "Metal fluorescence lidar (light detection and ranging) and the middle atmosphere," Contemp. Phys. **44**, 35–49 (2003).
28. C. S. Gardner and G. C. Papen, "Mesospheric Na wind/temperature lidar," Rev. Laser Eng. **23**, 131–134 (1995).
29. C. Y. She and J. R. Yu, "Simultaneous three-frequency Na lidar measurements of radial wind and temperature in the mesopause region," Geophys. Res. Lett. **21**, 1771–1774 (1994).
30. J. S. Friedman, C. A. Tepley, S. Raizada, Q. H. Zhou, J. Hedin, and R. Delgado, "Potassium Doppler-resonance lidar for the study of the mesosphere and lower thermosphere at the Arecibo Observatory," J. Atoms. Sol.-Terr. Phys. **65**, 1411–1424 (2003).
31. J. S. Friedman and X. Chu, "Nocturnal temperature structure in the mesopause region over the Arecibo Observatory (18.35°N, 66.75°W): Seasonal variations," J. Geophys. Res. **112**, D14107 (2007).
32. X. Chu, "Alexandrite-ring-laser-based Fe Doppler lidar for mobile/airborne deployment," in *Proceeding of the 23rd International Laser Radar Conference*, Nara, Japan (2006), pp. 385–388.
33. X. Chu, W. Huang, J. P. Thayer, Z. Wang, and J. A. Smith, "Progress in MRI Fe-Resonance/Rayleigh/Mie Doppler lidar," in *Proceeding of the 25th International Laser Radar Conference*, St. Petersburg, Russia (2010), pp. 947–950.
34. J. A. Gelbwachs, "Iron Boltzmann factor LIDAR: proposed new remote-sensing technique for mesospheric temperature," Appl. Opt. **33**, 7151–7156 (1994).
35. X. Chu, W. Pan, G. C. Papen, C. S. Gardner, and J. A. Gelbwachs, "Fe Boltzmann temperature lidar: design, error analysis, and initial results at the North and South Poles," Appl. Opt. **41**, 4400–4410 (2002).
36. S. Raizada and C. Tepley, "Iron Boltzmann lidar temperature and density observations from Arecibo — an initial comparison with other techniques," Geophys. Res. Lett. **29**, 1560 (2002).
37. K. H. Fricke and U. von Zahn, "Mesopause temperatures derived from probing the hyperfine structure of the D2 resonance line of sodium by lidar," J. Atmos. Terr. Phys. **47**, 499–512 (1985).
38. U. von Zahn and J. Höffner, "Mesopause temperature profiling by potassium lidar," Geophys. Res. Lett. **23**, 141–144 (1996).
39. J. Lautenbach and J. Höffner, "Scanning iron temperature lidar for mesopause temperature observation," Appl. Opt. **43**, 4559–4563 (2004).
40. J. Höffner and J. Lautenbach, "Daylight measurements of mesopause temperature and vertical wind with the mobile scanning iron lidar," Opt. Lett. **34**, 1351–1353 (2009).
41. C. S. Gardner, "Performance capabilities of middle-atmosphere temperature lidars: comparison of Na, Fe, K, Ca, $Ca^+$, and Rayleigh systems," Appl. Opt. **43**, 4941–4956 (2004).
42. M. L. Chanin, A. Garnier, A. Hauchecorne, and J. Porteneuve, "A Doppler lidar for measuring winds in the middle atmosphere," Geophys. Res. Lett. **16**, 1273–1276 (1989).
43. A. Garnier and M. Chanin, "Description of a Doppler rayleigh LIDAR for measuring winds in the middle atmosphere," Appl. Phys. B **55**, 35–40 (1992).
44. J. McKay, "Assessment of a multibeam Fizeau wedge interferometer for Doppler wind lidar," Appl. Opt. **41**, 1760–1767 (2002).
45. J. McKay and T. Wilkerson, "Direct Detection Doppler Lidar," Proc. SPIE **3127**, 42–52 (1997).
46. C.-Y. She, J. Yue, Z.-A. Yan, J. Hair, J.-J. Guo, S.-H. Wu, and Z.-S. Liu, "Direct-detection Doppler wind measurements with a Cabannes-Mie lidar: B. Impact of aerosol variation on iodine vapor filter methods," Appl. Opt. **46**, 4444–4454 (2007).
47. J. S. Friedman, C. A. Tepley, P. A. Castleberg, and H. Roe, "Middle-atmospheric Doppler lidar using an iodine-vapor edge filter," Opt. Lett. **22**, 1648–1650 (1997).
48. G. Baumgarten, "Doppler Rayleigh/Mie/Raman lidar for wind and temperature measurements in the middle atmosphere up to 80 km," Atmos. Meas. Tech. **3**, 1509–1518 (2010).
49. Z. S. Liu, W. B. Chen, T. L. Zhang, J. W. Hair, and C. Y. She, "An incoherent Doppler lidar for ground-based atmospheric wind profiling," Appl. Phys. B **64**, 561–566 (1997).
50. C.-Y. She, J. Yue, Z.-A. Yan, J. Hair, J.-J. Guo, S.-H. Wu, and Z.-S. Liu, "Direct-detection Doppler wind measurements with a cabannes-Mie lidar: A. comparison between iodine vapor filter and Fabry-Perot interferometer methods," Appl. Opt. **46**, 4434–4443 (2007).
51. O. Reitebuch, C. Lemmerz, E. Nagel, U. Paffrath, Y. Durand, M. Endemann, F. Fabre, and M. Chaloupy, "The airborne demonstrator for the direct-detection Doppler wind lidar ALADIN on ADM-aeolus. Part I: instrument design and comparison to satellite instrument," J. Atmos. Ocean. Technol. **26**, 2501–2515 (2009).
52. J. Hair, L. Caldwell, D. Krueger, and C.-Y. She, "High-spectral-resolution lidar with iodine-vapor filters: measurement of atmospheric-state and aerosol profiles," Appl. Opt. **40**, 5280–5294 (2001).
53. L. Mertz, "Wide-angle Mach-Zehnder interferometer for monochromatically selective photography," Appl. Opt. **16**, 812–813 (1977).
54. C. Grund, S. Tucker, R. Pierce, M. Ostasziewski, K. Kanizay, D. Demara, and J. Howell, "Development and demonstration of an optical autocovariance direct detection wind lidar," in *Earth Science Technology Forum*, Arlington, Virginia (2010).
55. X. Chu and W. Huang, "Fe Doppler-free spectroscopy and optical heterodyne detection for accurate frequency control of Fe-resonance Doppler lidar," in *Proceeding of the 25th International Laser Radar Conference*, St. Petersburg, Russia (2010), pp. 969–972.